Experimental and Numerical Investigation of Supersonic Turbulent Flow Through a Square Duct

D. O. Davis* and F. B. Gessner†
University of Washington, Seattle, Washington
and
G. D. Kerlick‡
Informatics General Corporation, NASA Ames Research Center, Moffett Field, California

Steady, developing, adiabatic, supersonic turbulent flow in a square duct is investigated for an inlet Mach number of 3.91 and a unit Reynolds number of 1.8×10^6/m. The experimental results indicate that two secondary flow cells develop about the corner bisector in a manner similar to that observed for the incompressible case. Numerical results based on the Baldwin-Lomax model show that this model is incapable of predicting turbulence-generated secondary flow cells. For a suitable choice of constants, the Gessner-Emery model is able to predict the strength of these cells, but is deficient with respect to predicting their positions in the flow and their distorting influence on the primary flow. These observations are based on comparisons made in this paper between predicted and measured total pressure contours, cross-flow velocity profiles, and local wall shear stress distributions.

Nomenclature

a = duct half width
c = speed of sound, $(\gamma p/\rho)^{\frac{1}{2}}$
c_p = specific heat at constant pressure
c_v = specific heat at constant volume
D = duct width or damping factor
e = total internal energy, $\rho h - p + \rho u_j u_j/2$
h = specific enthalpy
k = thermal conductivity
ℓ_b = Buleev's length scale
ℓ_p = Prandtl's length scale
L = duct length
M_i = inlet Mach number, u_i/c_i
p = static pressure
p_t = total pressure
P_r = Prandtl number, $\mu c_p/k$
Pr_t = turbulent Prandtl number
Re_i = inlet unit Reynolds number, u_i/v_i
t = time
u_1, u_2, u_3 = velocity components in the x_1, x_2, and x_3 directions, respectively
u_e = axial velocity component at boundary-layer edge
u_i = axial velocity component at inlet
u_r = resultant transverse velocity component, $(u_2^2 + u_3^2)^{\frac{1}{2}}$
u_τ = friction velocity, $(|\tau_w|/\rho_w)^{\frac{1}{2}}$
x_1, x_2, x_3 = Cartesian coordinates, see Fig. 1
γ = specific heat ratio, c_p/c_v
ϵ = eddy viscosity
v = kinematic viscosity
ρ = density
τ_{ij} = stress tensor
τ = shear stress
ω = mean vorticity

Superscripts

$\bar{(\ )}$ = time-averaged quantity
$\tilde{(\ )}$ = mass-averaged quantity
$(\ )'$ = time fluctuation
$(\ )''$ = mass-weighted fluctuation

Subscripts

e = boundary-layer edge condition
i = inlet condition
cl = centerline condition
w = wall condition

Received July 12, 1985; presented as Paper 85-1622 at the AIAA 18th Fluid Dynamics and Plasmadynamics and Lasers Conference, Cincinnati, OH, July 16-18, 1985; revision submitted Jan. 13, 1986.

*Graduate Research Assistant, Department of Mechanical Engineering.
†Professor, Department of Mechanical Engineering. Member AIAA.
‡Research Scientist, Applied Computational Aerodynamics Branch. Member AIAA.

Introduction

COMPRESSIBLE flow along a right-angled corner formed by two intersecting plates is one example of a relatively complex three-dimensional flow induced by a simple geometric configuration. For this particular situation, the three dimensionality of the flow is enhanced by the presence of cross flows in the near-wall layer that transport mass, momentum, and energy into and out of the corner region. Previous work in this area has generally focused on wedge-type corner flows that are intended to simulate supersonic engine inlet flows and flow along intersecting surfaces on flight vehicles.[1] Experimental data have been obtained for both laminar[2] and turbulent[3] flow conditions which show that a complex shock structure is generated by virtue of wave interactions in the corner region. The predictions of Shanker et al.[4] show that this shock structure is dominated by inviscid effects, rather than viscous effects, which serve primarily to shift the observed shock pattern outward as the displacement thickness increases. The more recent predictions of Shang et al.[5] show that the shock structure exhibits progressive changes in a manner which agrees with experimental observations as the flow undergoes transition and that discrete vortices are not formed in the corner region for either laminar or turbulent flow conditions.

The related problem of supersonic turbulent flow along a compression corner formed by a wedge positioned normal to a flat plate has also been addressed in some recent studies.[6-8] Numerical results presented by Hung and MacCormack[6] show

that velocity vectors in the flow immediately adjacent to the plate surface converge and diverge in a manner indicative of three-dimensional separation and reattachment near the line of intersection. Hung and Kurasaki[7] have shown that essentially the same results as those presented in Ref. 6 can be obtained if the thin-layer form of the Navier-Stokes equations is analyzed. Further refinements in terms of improved computational efficiency are possible if the hybrid explicit-implicit numerical algorithm developed by Knight[8] is utilized.

All of the above-mentioned studies have provided considerable insight into the nature of supersonic flow along an axial corner with one or more compression surfaces present. For these operating conditions, however, the flow structure is dominated by a complex shock wave pattern that tends to mask the effects of the turbulent field on local flow conditions in the corner region. Under these circumstances, it is difficult to assess the relative merits of any prescribed turbulence model, because the overall pattern is relatively insensitive to the specified model. The present study was undertaken, therefore, in order to examine the predictive capabilities of two turbulence models in common use today in a corner flow environment where Reynolds stress gradients dominate the local flowfield.

The selected flow situation is that of adiabatic, supersonic flow in a square duct that develops from a low-turbulence level, uniform axial mean flow at the duct inlet in the absence of strong internal shock waves. The two turbulence models tested are extended forms of the Baldwin-Lomax[9] and the Gessner-Emery[10] models. In previous related work, the Baldwin-Lomax model was utilized by Hung and MacCormack[6] and Knight[8] for wedge-plate-type corner flows and by Gorski et al.[11] who analyzed flow along a wing-body junction. Modified forms of the Gessner-Emery model were employed by Mikhail and Ghia[12] and Shang et al.[5] in order to investigate unbounded corner flows and intersecting wedge-type corner flows, respectively. In the present paper, numerical results based on these two models are compared with data generated from a companion experimental study in order to examine the predictive capabilities of each model more closely.

Conservation Equations

The starting point for the constitutive model is the time-dependent form of the conservation equations written in terms of mass-weighted variables. If order-of-magnitude approximations are applied, then time-averaged forms of the continuity, momentum, and energy equations and an equation of state can be written as[13]

Mass:

$$\frac{\partial \bar{\rho}}{\partial t} + \frac{\partial}{\partial x_j}(\bar{\rho}\tilde{u}_j) = 0 \tag{1}$$

Momentum:

$$\frac{\partial}{\partial t}(\bar{\rho}\tilde{u}_i) + \frac{\partial}{\partial x_j}\left[\bar{\rho}\tilde{u}_i\tilde{u}_j + \bar{p}\delta_{ij} - \left(\bar{\tau}_{ij} - \overline{\rho u_i'' u_j''}\right)\right] = 0 \tag{2}$$

Energy:

$$\frac{\partial \bar{e}}{\partial t} + \frac{\partial}{\partial x_j}\left[(\bar{p}+\bar{e})\tilde{u}_j - \frac{\mu}{Pr}\frac{\partial \tilde{h}}{\partial x_j} + \overline{\rho u_j'' h''} - \tilde{u}_i\left(\bar{\tau}_{ij} - \overline{\rho u_i'' u_j''}\right)\right] = 0 \tag{3}$$

Equation of state:

$$\bar{p} = (\gamma - 1)\left(\bar{e} - \tfrac{1}{2}\bar{\rho}\tilde{u}_i\tilde{u}_i\right) \tag{4}$$

where

$$\bar{\tau}_{ij} \equiv \mu\left[\left(\frac{\partial \tilde{u}_i}{\partial x_j} + \frac{\partial \tilde{u}_j}{\partial x_i}\right) - \frac{2}{3}\delta_{ij}\frac{\partial \tilde{u}_k}{\partial x_k}\right]$$

If $\bar{\rho}$, $\bar{p}$, $\bar{e}$, and $\tilde{u}_i$ are designated as the primary unknowns, then $\tilde{h}$, $\overline{\rho u_i'' u_j''}$, and $\overline{\rho u_j'' h''}$ must be expressed in terms of these variables in order to effect closure. An expression for $\tilde{h}$ can be developed by noting that for assumed ideal-gas behavior, $\bar{p} = (\gamma - 1)\overline{\rho h}/\gamma$, which, in conjunction with Eq. (4) and the defining relationship, $\tilde{h} = \overline{\rho h}/\bar{\rho}$, implies that

$$\tilde{h} = \gamma\left(\frac{\bar{e}}{\bar{\rho}} - \frac{1}{2}\tilde{u}_i\tilde{u}_i\right) \tag{5}$$

In accordance with common practice, the turbulence correlations $\overline{\rho u_i' u_j'}$ and $\overline{\rho u_j' h''}$ appearing in Eqs. (2) and (3) will be modeled in terms of mass-weighted variables by means of relationships analogous to those specifically developed for incompressible flow. This approach can be justified by first noting that Eqs. (1-3) reduce to appropriate forms for incompressible flow when the tilde is replaced by an overbar and when the double-primed quantities are replaced by single-primed quantities. If the reverse procedure is also assumed to be valid for empirically based relationships, then expressions of the form

$$\overline{\rho u_i' u_j'} = f_{ij}\left[\epsilon(\bar{u}_m, x_k), \bar{u}_m, x_k\right] \tag{6}$$

$$\overline{\rho u_j' h'} = \frac{\epsilon(\bar{u}_m, x_k)}{Pr_t}\frac{\partial \bar{h}}{\partial x_j} \tag{7}$$

imply relationships in terms of mass-weighted variables of the form

$$\overline{\rho u_i'' u_j''} = f_{ij}\left[\epsilon(\tilde{u}_m, x_k), \tilde{u}_m, x_k\right] \tag{8}$$

$$\overline{\rho u_j'' h''} = \frac{\epsilon(\tilde{u}_m, x_k)}{Pr_t}\frac{\partial \tilde{h}}{\partial x_j} \tag{9}$$

where ϵ is the eddy viscosity and Pr_t the turbulent Prandtl number.

Equations (8) and (9) can be justified more rigorously if it can be shown that these equations follow directly from Eqs. (6) and (7) on the basis of alternate arguments. For this purpose, it is expedient to examine certain identities that relate the mass-averaged variables to conventional time-averaged quantities, namely,[14]

$$\tilde{h} = \bar{h} + \overline{\rho' h'}/\bar{\rho} \tag{10}$$

$$\overline{\rho u_i'' u_j''} = \overline{\rho u_i' u_j'} - \overline{\rho' u_i'} \cdot \overline{\rho' u_j'}/\bar{\rho} \tag{11}$$

$$\overline{\rho u_j'' h''} = \overline{\rho u_j' h'} - \overline{\rho' h'} \cdot \overline{\rho' u_j'}/\bar{\rho} \tag{12}$$

$$\tilde{u}_i = \bar{u}_i + \overline{\rho' u_i'}/\bar{\rho} \tag{13}$$

For adiabatic, supersonic corner flows for which $\bar{M} < 5$ and $\bar{u}_1 \gg \bar{u}_2, \bar{u}_3$, where the velocity components are defined relative to the coordinate system shown in Fig. 1, it is reasonable to assume that total temperature and static pressure fluctuations are small in comparison to other fluctuations in the flow. These assumptions are logical extensions of the assumptions usually made when two-dimensional, adiabatic, supersonic boundary-layer flows are analyzed, and imply that[13]

$$\rho'/\bar{\rho} \simeq \alpha u_1'/\bar{u}_1 \tag{14}$$

and

$$h'/\bar{h} \simeq -\alpha u_1'/\bar{u}_1 \tag{15}$$

where $\alpha \equiv (\gamma - 1)\bar{M}^2$. If Eqs. (14) and (15) are substituted into Eqs. (10-13), then all of the correlations appearing on the right-hand sides of these equations are components of the Reynolds stress tensor. On the basis of Reynolds stress data obtained previously in two-dimensional, adiabatic, shock-free supersonic boundary-layer flows[15] and in incompressible square duct flows,[16] it is reasonable to assume that all Reynolds stress components are of the same order of magnitude in a typical supersonic corner flow. If the boundary-layer approximations are applied to this flow situation and triple correlations are assumed to be small in comparison to double correlations, then Eqs. (10-13) reduce to the following set of conditions:

$$\tilde{h} \simeq \bar{h} \tag{16}$$

$$\overline{\rho u_i'' u_j''} \simeq \overline{\rho u_i' u_j'} \quad (\text{all } i, j) \tag{17}$$

$$\overline{\rho u_j'' h''} \simeq \overline{\rho u_j' h'} \quad (\text{all } j) \tag{18}$$

$$\tilde{u}_1 \simeq \bar{u}_1 \tag{19}$$

$$\tilde{u}_2 \simeq \bar{u}_2 + \overline{u_1' u_2'}/\bar{u}_1 \tag{20}$$

$$\tilde{u}_3 \simeq \bar{u}_3 + \overline{u_1' u_3'}/\bar{u}_1 \tag{21}$$

Equations (16-19) show that $\bar{h}$, $\overline{\rho u_i' u_j'}$, $\overline{\rho u_j' h'}$, and $\bar{u}_1$ are essentially equivalent to $\tilde{h}$, $\overline{\rho u_i'' u_j''}$, $\overline{\rho u_j'' h''}$, and $\tilde{u}_1$, respectively, for adiabatic, supersonic corner flow. Equations (20) and (21) indicate, however, that $\tilde{u}_2 \neq \bar{u}_2$, $\tilde{u}_3 \neq \bar{u}_3$, which implies that $\epsilon(\tilde{u}_m, x_k) \neq \epsilon(\bar{u}_m, x_k)$, so that Eqs. (7) and (9) are not consistent. These results also imply that Eqs. (6) and (8) are not consistent with respect to the functional forms shown for $\overline{\rho u_i' u_j'}$ and $\overline{\rho u_i'' u_j''}$. These inconsistencies exist whenever $\overline{\rho u_i'' u_j''}$ is specified as a function of $\tilde{u}_1$, $\tilde{u}_2$, and $\tilde{u}_3$, as in the Baldwin-Lomax model, where the Boussinesq approximation is made and ϵ is modeled in terms of the mean vorticity. These inconsistencies vanish, however, if the Gessner-Emery model is utilized, because all of the Reynolds stress components in this model are expressed solely in terms of components of the primary mean rate of strain, namely $\partial \bar{u}_1/\partial x_2$ and $\partial \bar{u}_1/\partial x_3$. For this model, noting that $\tilde{u}_1 \simeq \bar{u}_1$ on the basis of Eq. (19), $\epsilon(\tilde{u}_1, x_k) \simeq \epsilon(\bar{u}_1, x_k)$, and the expressions for $\overline{\rho u_i' u_j'}$ and $\overline{\rho u_j' h'}$ given by Eqs. (6) and (7) are compatible with the mass-averaged forms for $\overline{\rho u_i'' u_j''}$ and $\overline{\rho u_j'' h''}$ given by Eqs. (8) and (9), respectively.

Although the above considerations do not validate Eqs. (8) and (9) as a means of modeling turbulent transport effects in terms of mass-averaged variables, they do provide some justification for using these equations to model the behavior of $\overline{\rho u_i'' u_j''}$ and $\overline{\rho u_j'' h''}$, inasmuch as they are equivalent to Eqs. (6) and (7), respectively, when ϵ and $\overline{\rho u_i'' u_j''}$ are modeled in terms of $\tilde{u}_1$ alone. When coupled with Eqs. (1-5), Eqs. (8) and (9) form a complete set of equations for analyzing adiabatic supersonic flow along a streamwise corner. In order to close this system of equations, the temperature dependency of μ was specified by means of Sutherland's formula in the present study and Pr and Pr_t were prescribed as 0.72 and 0.9, respectively.

Turbulence Models

Baldwin-Lomax Model

The Baldwin-Lomax model effects closure by coupling the Boussinesq approximation for $\overline{\rho u_i'' u_j''}$, namely

$$\overline{\rho u_i'' u_j''} = -\epsilon \left[\left(\frac{\partial \tilde{u}_i}{\partial x_j} + \frac{\partial \tilde{u}_j}{\partial x_i} \right) - \frac{2}{3} \delta_{ij} \frac{\partial \tilde{u}_k}{\partial x_k} \right] \tag{22}$$

with a prescribed two-layer model for ϵ where, for the inner layer,

$$\epsilon_i = \bar{\rho} (\kappa \ell_b D)^2 |\omega| \tag{23}$$

with the magnitude of the mean vorticity defined as

$$|\omega| \equiv (\Omega_k \Omega_k)^{1/2}, \quad \Omega_k = \epsilon_{ijk} \frac{\partial \tilde{u}_i}{\partial x_j} \tag{24}$$

and the Van Driest damping factor defined as

$$D \equiv 1 - \exp(-\ell_b u_\tau / A^+ \nu_w), \quad u_\tau = (|\tau_w|/\rho_w)^{\frac{1}{2}} \tag{25}$$

where τ_w, ρ_w, and ν_w are the local shear stress, density, and kinematic viscosity evaluated at the wall, respectively, and ℓ_b is the Buleev length scale.[17]

In unbounded corner flows, ℓ_b can be expressed in terms of position coordinates x_2 and x_3 (defined as shown in Fig. 1) as

$$\ell_b = \frac{2 x_2 x_3}{x_2 + x_3 + (x_2^2 + x_3^2)^{\frac{1}{2}}} \tag{26}$$

This equation can be applied without reservation to the entrance region of a square duct. After the wall boundary layers have merged, however, a modified form of Eq. (26) should be used to reflect the influence of all four walls on length-scale values in the flow [e.g., Eq. (97) in Ref. 17]. In the present study, Eq. (26) was used to specify length-scale behavior, inasmuch as the predictions were restricted to a development length over which the wall boundary layers had not yet merged ($0 \leq x_1/D \leq 20$).

For the outer region of the corner boundary layer, ϵ_o was specified as

$$\epsilon_o = \bar{\rho} k C_{cp} F_{\text{wake}} F_{\text{Kleb}} \tag{27}$$

where F_{wake} is the smaller of

$$F_{\text{wake}} = \ell_{b,\max} F_{\max}$$

$$F_{\text{wake}} = C_{wk} \ell_{b,\max} \bar{u}_e^2 / F_{\max} \tag{28}$$

$\bar{u}_e$ is the velocity at the boundary-layer edge, $\ell_{b,\max}$ is the value of ℓ_b when $\ell_b |\omega| D$ is a maximum, $F_{\max} = \ell_b |\omega| D$ at this condition, and

$$F_{\text{Kleb}} = \left[1 + 5.5 (C_{\text{Kleb}} \ell_b / \ell_{b,\max})^6 \right]^{-1} \tag{29}$$

Rather than attempting to match ϵ_i and ϵ_o values in the overlap region, both ϵ_i and ϵ_o were calculated at every point in the flow and the smaller value was used in Eq. (22) to determine the stress components. The coefficient values prescribed for this model are the same as those specified in the original model,[9] namely: $\kappa = 0.40$, $A^+ = 26$, $k = 0.0168$, $C_{cp} = 1.6$, $C_{\text{Kleb}} = 0.3$, and $C_{wk} = 0.2$.

Before discussing the Gessner-Emery model, some further comments are in order with respect to the weaknesses inherent in the form of Eq. (22) for streamwise corner flow calculations, regardless of the manner in which ϵ is specified. If the boundary-layer approximations for adiabatic, supersonic corner flow are applied, then $\overline{\rho u_2''^2}$, $\overline{\rho u_3''^2}$, and $\overline{\rho u_2'' u_3''}$ are each an order of magnitude less than either $\overline{\rho u_1'' u_2''}$ or $\overline{\rho u_1'' u_3''}$ on the basis of Eq. (22). This result is not likely to be in accord with reality, inasmuch as all five stress components should be of the same order of magnitude, because $\overline{\rho u_i'' u_j''} \simeq \overline{\rho u_i' u_j'}$ on the basis of earlier considerations and components of $\overline{u_i' u_j'}$ are all of the same order of magnitude in typical incompressible

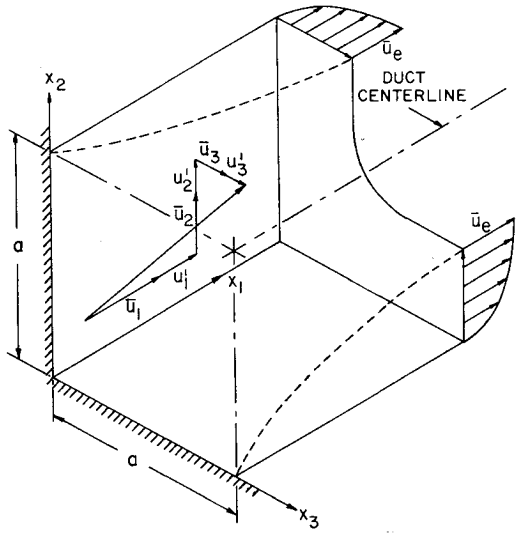

Fig. 1 Coordinate system and velocity components in relation to a duct quadrant.

corner flows.[16] Underestimating the magnitude of stress components involving the u_2'' and u_3'' fluctuations is likely to have serious consequences, inasmuch as gradients of $(\overline{\rho u_2''^2} - \overline{\rho u_3''^2})$ and $\overline{\rho u_2'' u_3''}$ are responsible for the generation of axial vorticity in the flow. If these gradients are underestimated, then Eq. (22) may not predict the cross-flow patterns actually present in the flow. Equation (22) is also deficient because the incompressible flow form of this equation, when applied to fully developed flow in a square duct, leads to the condition that $\bar{u}_2 = \bar{u}_3 = 0$ everywhere,[18] whereas experimental data show that well-defined secondary flow cells actually exist when the flow is fully developed.[16]

Gessner-Emery Model

The Gessner-Emery model is based on formal manipulation of the Reynolds stress transport equations with the convective and diffusive transport terms deleted. This model was developed specifically for incompressible flow in rectangular ducts of arbitrary aspect ratio[10] and has been applied to predict developing flow in square ducts with and without heat transfer present.[19,20] Stress component relationships referred to this model can be written in terms of mass-averaged variables and a two-component eddy viscosity as

$$\overline{\rho u_1''^2} = \frac{\alpha_1}{\alpha_2}\epsilon|\omega| \tag{30}$$

$$\overline{\rho u_2''^2} = -\frac{(2F_{12} + \alpha_1 - 2)}{\alpha_2}\epsilon_2\left|\frac{\partial \tilde{u}_1}{\partial x_2}\right| + \frac{F_{12}}{\alpha_2}\epsilon|\omega| \tag{31}$$

$$\overline{\rho u_3''^2} = -\frac{(2F_{12} + \alpha_1 - 2)}{\alpha_2}\epsilon_3\left|\frac{\partial \tilde{u}_1}{\partial x_3}\right| + \frac{F_{12}}{\alpha_2}\epsilon|\omega| \tag{32}$$

$$\overline{\rho u_1'' u_2''} = -\epsilon\frac{\partial \tilde{u}_1}{\partial x_2} \tag{33}$$

$$\overline{\rho u_1'' u_3''} = -\epsilon\frac{\partial \tilde{u}_1}{\partial x_3} \tag{34}$$

$$\overline{\rho u_2'' u_3''} = -\frac{(2F_{12} + \alpha_1 - 2)}{\alpha_2}\frac{\epsilon}{|\omega|}\frac{\partial \tilde{u}_1}{\partial x_2}\frac{\partial \tilde{u}_1}{\partial x_3} \tag{35}$$

where

$$\epsilon_2 = \bar{\rho}\ell_p^2\left|\partial \tilde{u}_1/\partial x_2\right| \tag{36}$$

$$\epsilon_3 = \bar{\rho}\ell_p^2\left|\partial \tilde{u}_1/\partial x_3\right| \tag{37}$$

$$\epsilon = \left(\epsilon_2^2 + \epsilon_3^2\right)^{1/2} = \bar{\rho}\ell_p^2|\omega| \tag{38}$$

with

$$|\omega| \equiv \left[\left(\frac{\partial \tilde{u}_1}{\partial x_2}\right)^2 + \left(\frac{\partial \tilde{u}_1}{\partial x_3}\right)^2\right]^{\frac{1}{2}} \tag{39}$$

where ℓ_p is Prandtl's length scale, whose spatial variation was prescribed by means of Eq. (8) in Ref. 10 using the modified coefficient values suggested by Gessner and Emery,[20] namely, $\alpha_1 = 0.26$, $\alpha_2 = 0.94$, and $F_{12} = 0.535$. For reasons that will be apparent shortly, computations were also performed with $F_{12} = 0.564$, which corresponds to the value suggested by the same authors in Ref. 10. This apparently slight modification in the numerical value for F_{12} results in a sixfold increase in the magnitude of $\overline{\rho u_2'' u_3''}$ and in the difference between $\overline{\rho u_2''^2}$ and $\overline{\rho u_3''^2}$, which implies a corresponding increase in the vorticity production term in the axial vorticity equation. For the prescribed coefficient values and the application at hand, the normal and shear stress components calculated from Eqs. (30-35) always satisfied the conditions: $\overline{\rho u_i'' u_j''} > 0$ when $i = j$ and $|\overline{\rho u_i'' u_j''}| < (\overline{\rho u_i''^2})^{\frac{1}{2}}(\overline{\rho u_j''^2})^{\frac{1}{2}}$ when $i \neq j$.

Physical Domain and Boundary Conditions

The physical domain is in the form of a rectangular prism having a cross-sectional area corresponding to one quadrant of a square duct, with a length bounded by the inlet and exit planes of the duct. At the duct inlet ($x_1 = 0$), $\tilde{u}_1$ was set equal to u_i, and $\tilde{u}_2 = \tilde{u}_3 = 0$ everywhere, which corresponds to a zero turbulence level, uniform axial mean flow at the duct inlet. Initial values of $\bar{\rho}$, $\bar{p}$, and $\bar{e}$ were calculated from specified total pressure, total temperature, and Mach number values at the inlet. The no-slip condition was applied to the three velocity components at the wall, and $\bar{\rho}$ and $\bar{e}$ at the wall were assumed to be equal to values calculated on the first mesh line adjacent to the wall, which was always well within the viscous sublayer. Equation (4) was then used to determine $\bar{p}$ at the wall by setting $\tilde{u}_i\tilde{u}_i = 0$. Along each wall bisector bounding the quadrant, a zero gradient condition in the normal direction was imposed on $\tilde{u}_1$, $\bar{\rho}$, $\bar{p}$, and $\bar{e}$. A zero or zero gradient condition was also imposed on $\tilde{u}_1$ and $\tilde{u}_3$ along each wall bisector, depending on the bisector under consideration. The exiting flowfield was fixed by specifying conditions in the last streamwise computational plane (located one mesh width downstream of the duct exit plane) as a linear extrapolation of calculated exit plane flow conditions.

Numerical Scheme

Numerical computations were performed using a modified form of the ARC-3D code developed by Pulliam and Steger,[21] which is a time-marching, implicit, finite difference procedure for solving the equations of motion for compressible flow in three dimensions. This technique was used to solve the equations of motion in strong conservation form after the thin-layer approximations had been applied. The computational grid consisted of a 31×31 mesh grid in the transverse plane, with mesh lines 30 in the x_2 and x_3 directions corresponding to the wall bisector locations, i.e., the lines of symmetry. A hyperbolic tangent function was used to cluster nodes near the duct walls and near the leading edge. More specifically, 24 nodes were clustered over the initial development length ($0 \leq x_1/D \leq 4.35$) and the downstream nodes were equally spaced at $\Delta x_1/D = 0.435$. In order to enhance numerical accuracy and efficiency, the calculations were performed relative to a transformed, spatially uniform grid, rather than with respect to the nonuniform grid in the physical domain.

All of the computations were performed on the Cray X-MP computer at the NASA Ames Research Center. Because of storage limitations, the computations had to be done incre-

mentally in the streamwise direction over sections composed of 25 mesh planes. The first section was initialized to the inlet conditions, while subsequent sections were initialized to the converged solution at the exit plane of the preceding section. Typically, for all cases, convergence of the calculations over the first section took 600-700 iterations, with subsequent sections requiring 400-500 iterations. The execution time per iteration for the Baldwin-Lomax and Gessner-Emery models was 2.8 and 3.4 s, respectively.

Experimental Configuration

The experimental facility used in the present study is a continuous flow, open-loop circuit with a test section in the form of a 20 in. (0.508 m) long square duct made of brass having a 1×1 in. (25.4×25.4 mm) cross section. This duct was centered within a larger, variable-area square duct made of plexiglass having a 2×2 in. (50.8×50.8 mm) cross section at the duct inlet, as shown in Fig. 2. The larger square duct was connected to an upstream convergent-divergent nozzle consisting of two contoured walls and two parallel side walls. This "duct within a duct" configuration was necessary in order to bypass the distorted boundary-layer flow on the nozzle side walls induced by the nonuniform nozzle expansion. To minimize wave reflection effects within the inner duct, shallow angle (2 deg) wedge sections were used to form the duct leading edge, as shown in Fig. 2. This particular configuration resulted in an essentially uniform axial mean flow at the inlet of the inner duct, which developed within the duct in the absence of strong internal shock waves. For the operating inlet Mach number ($M_i = 3.91$) and inlet unit Reynolds number ($Re_i = 1.8 \times 10^6$/m), turbulent boundary-layer development was initiated at, or very near, the duct leading edge. On the basis of previous surface temperature measurements with thermocouples embedded in the duct wall,[22] the flow developed adiabatically within the inner duct with a recovery factor approximately equal to 0.89.

The inner and outer duct flows exited as free jets into a test chamber immediately downstream of the duct exit plane. Approximately one outer duct width downstream, both jet flows were recaptured by an in-line diffuser positioned within the test chamber. This diffuser had a variable-area second throat outside the test chamber that was adjusted in order to match the test chamber pressure to the static pressure at the exit of the inner duct. Variable-length friction plates between the inner and outer ducts, positioned as shown in Fig. 2, were used to match the static pressure of the inner and outer duct flows at the exit plane. In this manner, it was possible to effect a three-way match in static pressure in order to avoid expansion or compression waves immediately downstream of the exit plane. This was done to minimize the possibility of local corner flow separation and/or spurious effects on the inner duct flow near the exit plane, where total pressure and mean velocity data were obtained by means of forward-facing pitot tubes and yaw angle (Conrad) probes located within the test chamber. Details of the flow facility, probe configurations, measurement techniques, and data reduction procedures are described by Lo[22] and Davis[23] and are given in a related paper that presents additional experimental results.[24]

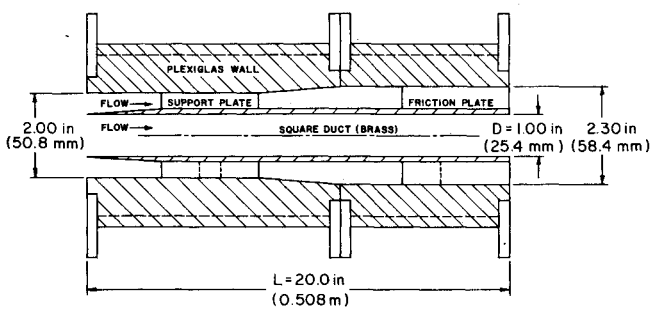

Fig. 2 Experimental test section, $L/D = 20$.

Experimental and Numerical Results

Total pressure contours and horizontal cross-flow component distributions measured at $x_1/D = 20$ are shown in Figs. 3 and 4, respectively. The symmetric undulation appearing in the contour $\bar{p}_t/\bar{p}_{t,cl} = 0.95$ was measured in each of the other three quadrants and is the result of reflected Mach waves in the flow induced by the combined effects of streamline deflection at the duct leading edge and displacement thickness growth along the duct. The undulations in the contour $\bar{p}_t/\bar{p}_{t,cl} = 0.1$ are indicative of the presence of two contrarotating secondary flow cells centered about the corner bisector. The presence of these cells was inferred on the basis of the following considerations.

A Conrad probe designed to minimize total pressure gradient effects was used to measure the horizontal cross-flow component distributions. The distributions measured by this probe at selected points in the lower octant ($x_2 < x_3$) at $x_1/D = 20$ are shown in Fig. 4. These distributions are indicative of the presence of a counterclockwise vortex in the lower

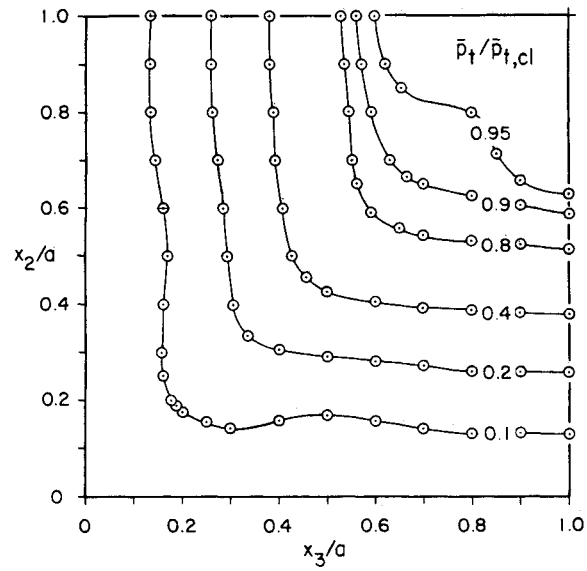

Fig. 3 Measured total pressure contours at $x_1/D = 20$.

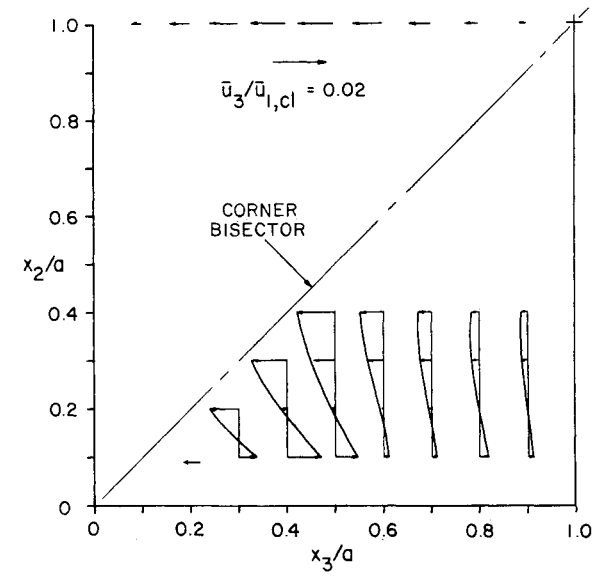

Fig. 4 Measured cross flow distributions at $x_1/D = 20$.

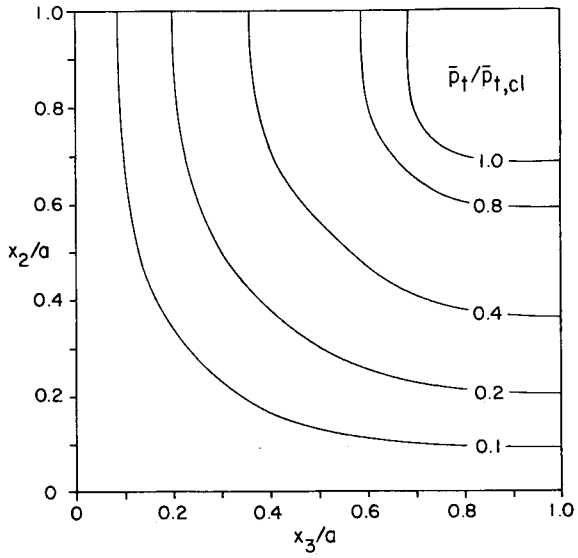

a) Baldwin-Lomax model.

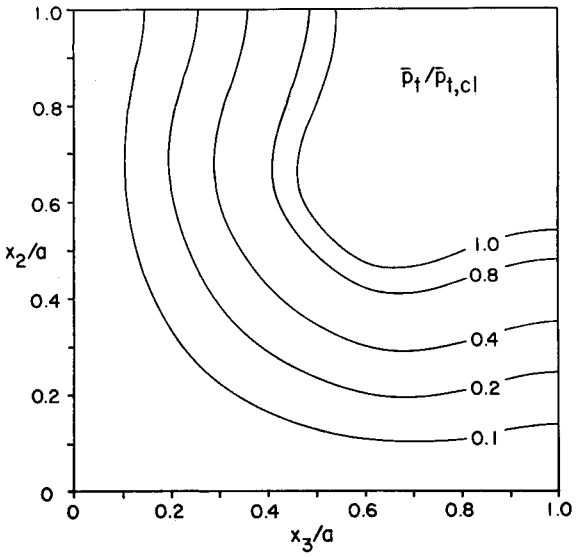

b) Gessner-Emery model, $F_{12} = 0.535$.

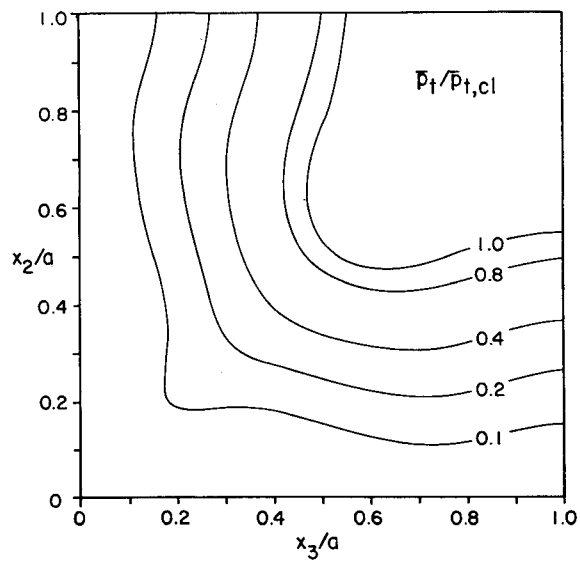

c) Gessner-Emery model, $F_{12} = 0.564$.

Fig. 5 Predicted total pressure contours at $x_1/D = 20$.

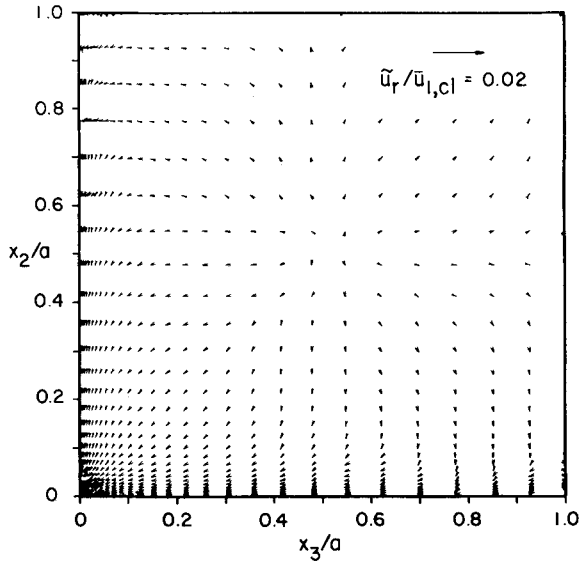

a) Baldwin-Lomax model.

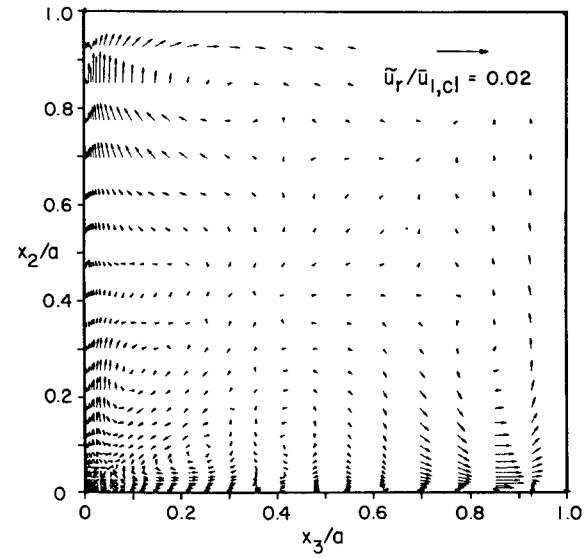

b) Gessner-Emery model, $F_{12} = 0.535$.

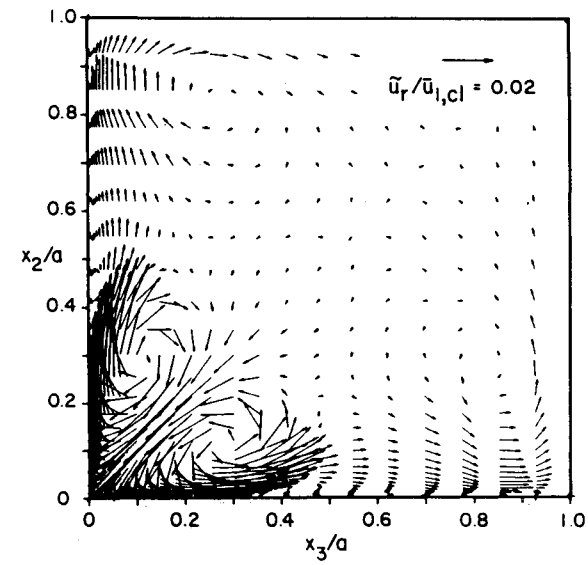

c) Gessner-Emery model, $F_{12} = 0.564$.

Fig. 6 Predicted cross flow vectors at $x_1/D = 20$.

octant, which, on the basis of symmetry about the corner bisector, implies the existence of a clockwise vortex in the upper octant ($x_2 > x_3$). Cross-flow data taken by Davis[23] with additional duct sections in series with the test section shown in Fig. 2 indicate that these vortices grow in lateral extent beyond $x_1/D = 20$ until they extend across the entire quadrant at $x_1/D = 40$, where transverse flow along the wall bisector $x_2/a = 1$ is directed away from the wall, rather than toward the wall, as shown in Fig. 4. It should be noted here that the total pressure contours and cross-flow profiles shown in Figs. 3 and 4 are similar in appearance to distributions that have been measured in incompressible square duct flow at approximately the same streamwise location.[25,26]

Predicted total pressure contours and cross-flow profiles based on the Baldwin-Lomax and Gessner-Emery turbulence models are shown in Figs. 5 and 6, respectively. These results are directly comparable to the experimental results shown in Figs. 3 and 4 with one qualification. Whereas the experimental results in Fig. 4. show the behavior of the conventional, time-averaged cross-flow components ($\bar{u}_2$ and $\bar{u}_3$), the predicted results in Fig. 6 show the behavior of the vector sum of the mass-weighted cross-flow components ($\tilde{u}_2$ and $\tilde{u}_3$). In reference to Eq. (13), these components are not equivalent because $\overline{\rho' u_i'} (i = 2,3)$ is nonzero in supersonic, turbulent square duct flow. On the basis of turbulence data obtained by Rose[27] in an axisymmetric supersonic boundary layer, however, it is estimated that $\tilde{u}_2$ and $\tilde{u}_3$ differ by no more than 20% from $\bar{u}_2$ and $\bar{u}_3$, respectively, so that horizontal component distributions of the transverse flow patterns shown in Fig. 6 should be qualitatively similar to the experimental profiles shown in Fig. 4 if the corresponding turbulence model is performing properly.

Comparison of Figs. 5a and 6a with the experimental results shown in Figs. 3 and 4 indicates that the Baldwin-Lomax model is unable to predict observed cross-flow behavior in supersonic square duct flow and, in turn, its distorting influence on the total pressure contours in the corner region. The Gessner-Emery model with $F_{12} = 0.535$ yields only very weak secondary flow cells in the near vicinity of the corner (Fig. 6b) and essentially no distortion of total pressure contours in this region (Fig. 5b). When F_{12} is increased to 0.564 (which, as noted earlier, corresponds to an increase in the generation of axial vorticity in the flow), the strength of the two secondary flow cells centered about the corner bisector increases markedly (Fig. 6c). For both cases ($F_{12} = 0.535$ and 0.564), there is also a relatively strong cross flow in the near-wall layer directed away from the corner, which turns outward in the vicinity of the wall bisectors to form a weak vortex near each bisector (Figs. 6b and 6c). In reference to the limited number of profiles shown in Fig. 4, it is not possible to determine whether these additional vortices are present in the actual flow. When $F_{12} = 0.564$, the strength of the secondary flow cells in the vicinity of the corner bisector is comparable in magnitude to that implied by the experimental profiles in Fig. 4. There is also an associated increase in the distortion of total pressure contours in the near vicinity of the corner (Fig. 5c) similar to that shown in Fig. 3 for the experimental contours. It should be noted, however, that predicted secondary flow cells based on $F_{12} = 0.564$ are positioned too close to the corner (Fig. 6c) in comparison to the cell structure implied by the experimental profiles shown in Fig. 4. This same type of shortcoming was observed by Gessner and Emery,[20] who attributed discrepancies between their predictions and secondary flow profiles measured in incompressible square duct flow to the exclusion of transport effects in their algebraic stress model.

Predicted axial wall static pressure distributions are compared with values measured along two intersecting walls of the duct in Fig. 7. From the figure it is evident that undulations exist in both the predicted and measured distributions, with stronger undulations present in the experimental distribution.

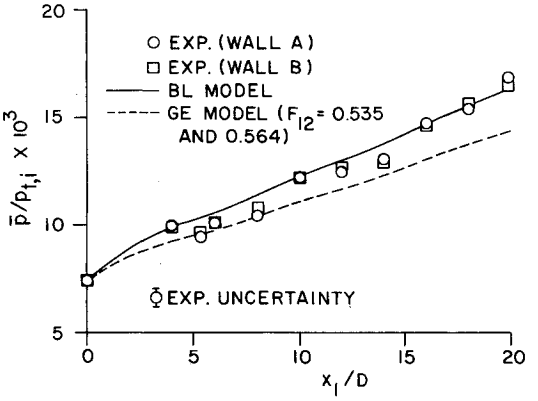

Fig. 7 Comparison of predicted and measured axial wall static pressure distributions.

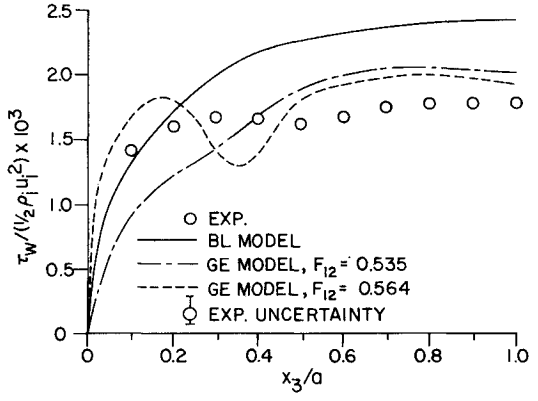

Fig. 8 Comparison of predicted and measured spanwise wall shear stress distributions at $x_1/D = 20$.

These undulations are caused by the reflection of weak shock waves generated at the duct leading edge and the reflection of Mach waves generated by the displacement thickness growth along the duct. The stronger undulations associated with the experimental distribution appear to indicate that the strength of the leading-edge shock waves is enhanced to some extent by the slight bluntness of the leading edge, an effect not present in the idealized configuration used for the computations. Figure 7 also shows that the Baldwin-Lomax model yields wall static pressure values which increase more rapidly than those predicted by the Gessner-Emery model. This behavior is directly attributable to a more rapid displacement thickness growth predicted by the Baldin-Lomax model, an effect implied by the relative positioning of the total pressure contours shown in Fig. 5a in comparison to that shown in Figs. 5b and 5c.

The predicted and measured spanwise variation of the local wall shear stress at $x_1/D = 20$ is shown in Fig. 8. Each experimental data point represents the average value of three values measured by means of different diameter Preston tubes. These data were reduced by applying the calibration equation suggested by Bradshaw and Unsworth[28] for reasons discussed by Davis.[23] In reference to Fig. 8, the experimental distribution has a minimum value at $x_3/a = 0.5$, which is compatible with the local peaking of the total pressure contour $\bar{p}_t/p_{t,cl} = 0.1$ at $x_3/a = 0.5$ shown in Fig. 3. This distribution is not modeled well by either the Baldwin-Lomax or Gessner-Emery model with $F_{12} = 0.535$, however, because neither model adequately predicts experimentally observed secondary flow behavior at $x_1/D = 20$ (compare Figs. 6a and 6b with Fig. 4). The predicted distribution based on the Gessner-Emery model with $F_{12} = 0.564$ does exhibit a local minimum near $x_3/a =$

0.35, but the undulations present in this distribution are overly accentuated in comparison to those existing in the experimental distribution. This effect could possibly be minimized by selecting an alternate value for F_{12} between the values considered in the present study (0.535 and 0.564). This maneuver would not completely eliminate discrepancies between predictions and experiment, however, because predicted wall shear stress values would still lie above their experimental counterparts when $x_3/a \geq 0.5$ (refer to Fig. 8). The experimentally observed local minimum at $x_3/a = 0.5$ would also not be predicted by a simple change in value for F_{12} because, as noted earlier, predicted secondary flow cells are positioned too close to the corner when $0.535 \leq F_{12} \leq 0.564$, so that the distorting influence of secondary flow on local wall shear stress distributions will be similarly confined to the near-corner region.

Conclusions

The nature of a supersonic turbulent flow that develops within a square duct from a low turbulence level, uniform axial mean flow condition at the duct inlet has been investigated both experimentally and numerically. The experimental results show that two secondary flow cells develop about the corner bisector in a manner similar to that observed for incompressible square duct flow. This secondary flow distorts total pressure contours and causes spanwise undulations in local wall shear stress distributions.

The Baldwin-Lomax model is unable to predict the development of secondary flow cells in supersonic turbulent square duct flow and, in turn, the distorting influence of these cells on the primary flow. The Gessner-Emery model with $F_{12} = 0.535$ yields only marginal improvements, because it underestimates the strength of the secondary flow and the degree of distortion present in the primary flow. When F_{12} is increased to 0.564 in the Gessner-Emery model, the strength of the predicted secondary flow cells is comparable to that observed experimentally, but total pressure contours and local wall shear stress distributions are overly distorted in comparison to their experimental counterparts in the near-corner region. Inasmuch as the selection of an alternate value for F_{12} will not cure these problems, it appears that a higher-order (e.g., two-equation) closure model will be necessary in order to model experimentally observed features of the flow more accurately. The feasibility of this approach will be explored in future work.

Acknowledgments

Funds for the support of this study have been allocated by the NASA Ames Research Center, Moffett Field, CA, under Interchange NCA2-1R850-401.

References

[1] Korkegi, R.H., "Survey of Viscous Interactions Associated with High Mach Number Flight," *AIAA Journal*, Vol. 9, May 1971, pp. 771-784.

[2] Charwat, A.F. and Redekeopp, L.G., "Supersonic Interference Flow Along the Corner of Intersecting Wedges," *AIAA Journal*, Vol. 5, March 1967, pp. 480-488.

[3] West, J.E. and Korkegi, R.H., "Supersonic Interaction in the Corner of Intersecting Wedges at High Reynolds Numbers," *AIAA Journal*, Vol. 10, May 1972, pp. 652-656.

[4] Shankar, V., Anderson, D., and Kutler, P., "Numerical Solutions for Supersonic Corner Flow," *Journal of Computational Physics*, Vol. 17, 1975, pp. 160-180.

[5] Shang, J.S., Hankey, W.L., and Petty, J.S., "Three-Dimensional Supersonic Interacting Flow Along a Corner," *AIAA Journal*, Vol. 17, July 1979, pp. 706-713.

[6] Hung, C.M. and MacCormack, R.W., "Numerical Solution of Three-Dimensional Shock Wave and Turbulent Boundary-Layer Interaction," *AIAA Journal*, Vol. 16, Oct. 1978, pp. 1090–1096.

[7] Hung, C.M. and Kurasaki, S.S., "Thin-Layer Approximation for Three-Dimensional Supersonic Corner Flows." *AIAA Journal*, Vol. 18, Dec. 1980, pp. 1544-1546.

[8] Knight, D.D., "A Hybrid Explicit-Implicit Numerical Algorithm for the Three-Dimensional Compressible Navier-Stokes Equations," *AIAA Journal*, Vol. 22, Aug. 1984, pp. 1056-1063.

[9] Baldwin, B.S. and Lomax, H., "Thin Layer Approximation and Algebraic Model for Separated Turbulent Flows," AIAA Paper 78-257, Jan. 1978.

[10] Gessner, F.B. and Emery, A.F., "A Length-Scale Model for Developing Turbulent Flow in a Rectangular Duct," *Journal of Fluids Engineering*, Vol. 99, June 1977, pp. 347-356.

[11] Gorski, J.J., Govidan, J.R., and Lakshminarayana, B., "Computation of Three-Dimensional Turbulent Shear Flows in Corners," *AIAA Journal*, Vol. 23, May 1985, pp. 685-692.

[12] Mikhail, A.G. and Ghia, K.N., "Analysis and Asymptotic Solutions of Compressible Turbulent Corner Flow," *Transactions of ASME, Journal of Engineering for Power*, Vol. 104, July 1982, pp. 571-579.

[13] Cebeci, T. and Smith, A.M.O., *Analysis of Turbulent Boundary Layers*, Academic Press, New York, 1974, pp. 62-80.

[14] Rubesin, M.W. and Rose, W.C., "The Turbulent Mean-Flow, Reynolds-Stress, and Heat-Flux Equations in Mass-Averaged Dependent Variables," NASA TM X-62248, March 1973.

[15] Fernholz, H.H., Finley, P.J., and Mikulla, V., "A Further Complication of Compressible Boundary Layer Data with a Survey of Turbulence Data," AGARDograph 263, Nov. 1981.

[16] Brundrett, E. and Baines, W.D., "The Production and Diffusion of Vorticity in Duct Flow," *Journal of Fluid Mechanics*, Vol. 19, 1964, pp. 375-394.

[17] Buleev, N.I., "Theoretical Model of the Mechanism of Turbulent Exchange in Fluid Flows," Atomic Energy Research Establishment, Harwell, England, AERE Translation 957, 1963.

[18] Fillo, J.A., "Transverse Velocities in Fully Developed Duct Flows," *The Physics of Fluids*, Vol. 17, Sept. 1974, pp. 1778-1779.

[19] Emery, A.F., Neighbors, P.K., and Gessner, F.B., "The Numerical Prediction of Developing Turbulent Flow and Heat Transfer in a Square Duct," *Journal of Heat Transfer*, Vol. 102, Feb. 1980, pp. 51-57.

[20] Gessner, F.B. and Emery, A.F., "The Numerical Prediction of Developing Turbulent Flow in Rectangular Ducts," *Journal of Fluids Engineering*, Vol. 103, Sept. 1981, pp. 445-455.

[21] Pulliam, T.H. and Steger, J.L., "Implicit Finite-Difference Simulations of Three-Dimensional Compressible Flow," *AIAA Journal*, Vol. 18, Feb. 1980, pp. 159-167.

[22] Lo, C.H., "Mean Flow Measurements in a Square Duct for Supersonic Turbulent Flow Conditions," M.S. Thesis, Dept. of Mechanical Engineering, University of Washington, Seattle, 1982.

[23] Davis, D.O., "Experimental and Numerical Investigation of Steady, Supersonic, Turbulent Flow Through a Square Duct," Thesis, Dept. of Mechanical Engineering, University of Washington, Seattle, 1985.

[24] Gessner, F.B., Ferguson, S.D., and Lo, V.C., "Experiments on Supersonic Turbulent Flow Development in a Square Duct," AIAA Paper 86-1038, May 1986.

[25] Melling, A., "Investigation of Flow in Non-Circular Ducts and Other Configurations by Laser Doppler Anemometry," Ph.D. Thesis, University of London, London, 1975 (see also *Journal of Fluid Mechanics*, Vol. 78, 1976, pp. 289-315).

[26] Gessner, F.B., Po, J.K., and Emery, A.F., "Measurements of Developing Turbulent Flow in a Square Duct," *Turbulent Shear Flows I*, Springer-Verlag, New York, 1979, pp. 119-136.

[27] Rose, W.C., "The Behavior of a Compressible Turbulent Boundary Layer in a Shock-Wave-Induced Adverse Pressure Gradient, Ph.D. Thesis, Dept. of Mechanical Engineering, University of Washington, Seattle, 1972 (see also NASA TN D-7092, March 1973).

[28] Bradshaw, P. and Unsworth, K., "Comment on 'Evaluation of Compressible Flow Preston Tube Calibrations,'" *AIAA Journal*, Vol. 12, Sept. 1974, pp. 1293-1295.